LASER & PHOTONICS REVIEWS

www.lpr-journal.org

Direct Imprinting of Laser Field on Halide Perovskite Single Crystal for Advanced Photonic Applications

A. Y. Zhizhchenko, A. B. Cherepakhin, M. A. Masharin, A. P. Pushkarev, S. A. Kulinich, A. P. Porfirev, A. A. Kuchmizhak, and S. V. Makarov**

Single crystal halide perovskites with microscale dimensions are an emerging class of objects for various advanced photonic and optoelectronic applications. Particularly, defect tolerance and broadband tunability of luminescence make them one of the most prospective candidates to develop microlasers for visible range. However, their post-processing by standard nanolithography methods face a number of problems related to worsening of their properties, thus making gentle laser processing one of best solutions for perovskite patterning. Here, it is shown that femtosecond laser irradiation of single-crystal halide perovskite $CsPbBr_3$ allows for its precise and ultraclean ablation fully controlled at subwavelength scale by the intensity and polarization distribution of the complex laser field applied. Indeed, the extremely low thermal conductivity (over 300 times lower than that of silicon) and ultrafast thermalization rate makes it possible to reduce heat-affected zone and avoid melting layer contribution, while the high refractive index (larger than 2) provides high spatial resolution in case of irradiation of pre-patterned focusing perovskite nanostructures. These features allow for direct imprinting of the incident laser field at wavelength $\lambda = 515$ nm, creating micro-lens and various light-emitting metasurfaces with deeply subwavelength spatial resolution (down to $\lambda/7$).

1. Introduction

Halide perovskites represent a promising class of materials for advanced photonic and optoelectronic applications.[1,2] Fast and simple wet-chemistry approaches allow for creation of various micro- and nanoscale single crystals from these materials, which are of high demand for micro- and nano-optics.[3–18] At the same time, large-scale and low-cost methods for fabrication of nano- and microstructures from halide perovskite films would enable neutral- and multi-colored semi-transparency for building-integrated photovoltaics,[19,20] tandem solar cells,[21] light-emitting devices,[22] and lasers.[23] In this regard, development of high-throughput methods for nanopatterning and processing of perovskites without irreversible decay of their luminescent and charge-carriers transport properties is highly anticipated.

Direct femtosecond (fs) laser ablation withstands as a high-throughput, simple, and chemically clean method of surface nanopatterning that was successfully applied for gentle and precise micro- and nanostructuring of various materials.[24–28] However, most of conventional semiconductors possess relatively high thermal conductivity ($\approx 10^{-1}$–10^{1} W cm^{-1}·K^{-1}), which limits the precision and functionality of surface ablation via heat transfer that proceeds at a length scale of ≈0.1–1 μm. Such ultrafast thermal processes lead to defect generation and development of surface instabilities, as laser ablation typically leaves damaged material with random surface morphology and heat-affected optical and optoelectronic properties.[29] In turn, halide perovskites with their extremely low thermal conductivity ($\kappa \approx 10^{-3}$ W cm^{-1} K^{-1}[30]) and high defect tolerance represent semiconductor materials in which the above mentioned thermal issues arising in the process of direct laser nanostructuring

A. Y. Zhizhchenko, S. A. Kulinich, A. A. Kuchmizhak
Pacific Quantum Center
Far Eastern Federal University
6 Sukhanova Str., Vladivostok 690061, Russia
E-mail: alex.iacp.dvo@mail.ru

A. Y. Zhizhchenko, A. B. Cherepakhin, A. A. Kuchmizhak
Institute of Automation and Control Processes
Far Eastern Branch
Russian Academy of Science
Vladivostok 690041, Russia

M. A. Masharin, A. P. Pushkarev, S. V. Makarov
School of Physics and Engineering
ITMO University
St. Petersburg 197101, Russia
E-mail: s.makarov@metalab.ifmo.ru

S. A. Kulinich
Research Institute of Science and Technology
Tokai University
Hiratsuka, Kanagawa 259-1292, Japan

A. P. Porfirev
Image Processing Systems Institute of RAS – Branch of the FSRC "Crystallography and Photonics" RAS
Samara 443001, Russia

The ORCID identification number(s) for the author(s) of this article can be found under https://doi.org/10.1002/lpor.202100094

DOI: 10.1002/lpor.202100094

can be successfully overcame. Indeed, direct laser processing of halide perovskites was recently employed for solar cell scribing, fabrication of functional micro-optics (diffraction gratings, Fresnel lenses, etc.), as well as for non-destructive imprinting of microlasers.[31–38] Efficient coupling of laser energy into perovskite material realized via artificially designed complex light fields is expected to drive further progress in this area permitting to minimize thermal impact on material properties and reach deep subwavelength spatial resolution required for fabrication of functional designs.

In this work, we demonstrate precise and ultra-clean fabrication of various functional micro- and nanostructures via direct imprinting of complex fs-laser fields in inorganic ($CsPbBr_3$) halide perovskite single crystals. First, we shed light onto the origins of delicate and precise laser-induced material removal from the perovskite crystal surface by comparing ablation thresholds and laser thermalization processes with those for well-studied monocrystalline silicon processed under similar conditions. Second, based on the developed approach, we then demonstrate single-pulse fabrication of ultra-smooth high-NA focusing micro-optical elements, parabolic microlenses and truncated microaxicons. Finally, we show fabrication of various advanced nanophotonic designs via direct ablation of prepatterned $CsPbBr_3$ surface with a spatial resolution down to $\lambda/7$ at $\lambda = 515$ nm. Management over the intensity and polarization of the laser fields permits to control the ablation behavior at deep subwavelength scale with results that can be predicted by full-wave electromagnetic modeling.

2. Results and Discussion

We started by systematically studying direct fs-laser ($\lambda = 515$ nm, pulse width =180 fs) ablation of ITO-supported monocrystalline $CsPbBr_3$ microplates (**Figure 1**a). Fabrication details of such perovskite microplates can be found in the Supporting Information. Laser radiation was focused on the microplate surface using a dry lens with a numerical aperture NA = 0.8 yielding a focal spot of D_{opt}=1.22λ/NA ≈ 0.78 µm. Single-pulse ablation of the microplates with a thickness of several microns was found to leave smooth concave-shaped microcraters on their surface. Both the size of such a crater D and its depth were found to increase along laser fluence F as illustrated in Figure 1b. At the same time, at fixed laser fluence, the microcrater geometry was found to be perfectly reproducible from pulse to pulse (see Supporting Information).

The choice of the fs-laser wavelength is dictated by the following reasons. Perovskite microcrystals are highly transparent within a certain spectral range (e.g., $CsPbBr_3$ is transparent at wavelength larger than 530 nm; see Supporting Information for transmittance and dispersion as well as data from ref. [12]), which means the laser processing of such material will be wavelength-dependent. In particular, near-IR radiation (that corresponds to fundamental harmonics of common fs-laser systems), the perovskite is expected to show multiphoton absorption and ablation behavior common for dielectric materials. In this respect, transparency of the material will allow to focus the laser radiation below its surface ensuring high-resolution laser recording inside the bulk of the perovskite microcrystals via multi-photon absorption processes. Decrease of the fs-laser wavelength to UV range allows to shrink the lateral size of the laser focal spot potentially ensuring increase of the processing resolution, yet UV fs-laser pattering is more expensive. Being compared to the IR- or UV-range pulses, second-harmonic visible-range radiation (as those used in our work) provides good trade-off between wavelength-dependent focusing capabilities and facile handling.

Surface ablation of a semiconductor by fs-laser pulses is a complex phenomenon that involves several atomic-scale processes such as electron-hole pairs excitation, their thermalization, thermal diffusion, phase transitions, shock wave generation, ultrafast cooling, etc. All these dramatically affect the final morphology of irradiated surface. Rigorous analysis of all involved processes is expected to be extremely complicated taking into account the complex chemical composition of the perovskite microplates and lack of reference data regarding their physical, optical and nonlinear optical characteristics. To shed light on the complex physics of perovskite ablation, by systematically measuring the size of laser-printed crater (D) versus applied fluence F, we first obtained the corresponding threshold fluence $F_{th} \approx 20$ mJ cm^{-2} for single-pulse $CsPbBr_3$ ablation (see orange markers in Figure 1c). To calibrate the obtained value, similar ablation experiments were carried out with a monocrystalline silicon substrate (c-Si), an extensively studied semiconductor material, revealing corresponding $F_{th} \approx 130$ mJ cm^{-2} (purple markers in Figure 1c), which is consistent with the literature data.[39] Comparative SEM study of crater morphology on the surface of both materials reveals advantages of fs-laser ablation of the $CsPbBr_3$: i) absence of debris (nanoparticles) near or inside microcrater and ii) absence of a rim formed by laser-melted material (Figure 1d).

In order to clarify the origin of such gentle ablation of $CsPbBr_3$, we extract experimental values of the characteristic diameters (σ) of laser energy deposition to the perovskite and c-Si surface. As shown in Figure 1c, the linear slope of experimental dependencies $D^2 = \sigma^2 \ln(F/F_{th})$ yields σ_{Si}=0.95 µm and $\sigma_{CsPbBr3}$=0.8 µm for the same focusing conditions. Generally, $\sigma = \sqrt{D_{opt}^2 + (2L_T)^2}$, where $D_{opt} = 1.22\lambda/NA$ is the "optical diameter" and $L_T \propto \kappa \cdot \tau$ is the characteristic length scale responsible for spreading of the laser-modified area via thermal diffusion in the material (where κ is the material's thermal conductivity and τ is characteristic thermalization time; see inset of Figure 1a). By comparing the measured slopes with the focal spot size D_{opt}, one can estimate L_T(Si) = 0.23 µm, which agrees with previously reported studies.[40] In a sharp contrast, for $CsPbBr_3$ perovskite $L_T(CsPbBr_3) \approx 0$ µm, which indicates near-zero thermal transport in the laser-irradiated material and helps to explain the gentle ablation and formation of extremely smooth microcraters observed.

Indeed, L_T also contributes to the heat penetration depth, being an additional term to the optical penetration depth L_{opt} that is inversely proportional to the absorption coefficient α. For our irradiation conditions, $L_{opt}(Si) = 1/\alpha = 670$ nm[41] and $L_{opt}(CsPbBr_3) = 100$ nm,[12] for silicon and perovskite materials, respectively. In the very beginning, absorption of laser pulse energy leads to the formation of electron-hole pairs. Both irradiated materials are highly absorbing, so their photogenerated electron-hole plasma density can be estimated taking into account only single-photon interband absorption expressed as $N_{eh} = \alpha F(1-R)/\hbar\omega$, where R is the reflectance and ω is the

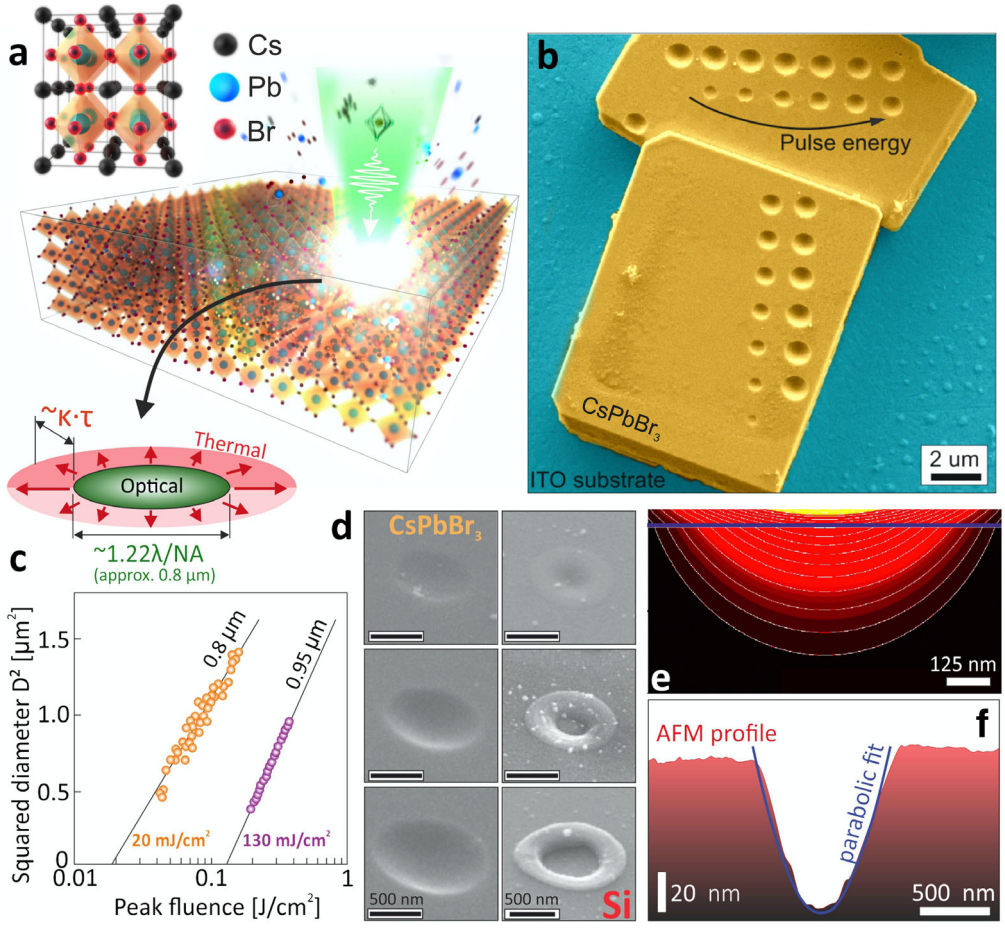

Figure 1. Direct fs-laser processing of $CsPbBr_3$ micro-crystals. a) Schematic illustration of single-pulse ablation of $CsPbBr_3$. Atomic structure of this material is illustrated in the top inset. The bottom inset provides details on optical and thermal contributions to the lateral size of the ablated area, where κ and τ indicate thermal conductivity and characteristic thermalization time, respectively. b) False-color SEM image showing concave-shaped microcraters produced on the surface of $CsPbBr_3$ micro-crystals by single-pulse ablation at elevating fluence F. c) Squared lateral size (D^2) of the concave crater produced on the surface of $CsPbBr_3$ (orange) and monocrystalline Si (purple) as a function of the peak laser fluence F. Linear fit of both data sets gives the threshold ablation fluence F_{th} of 20 and 130 mJ cm^{-2} and lateral energy deposition scales σ of 0.8 and 0.95 μm for $CsPbBr_3$ and Si, respectively. d) Side-view SEM images comparing surface morphology of single-pulse craters produced in $CsPbBr_3$ and Si at elevating fluence (from 40 to 100 mJ cm^{-2} for $CsPbBr_3$ and from 200 to 400 mJ cm^{-2} for Si). e) Calculated squared electric-field amplitude $|E(r,z)|^2$ near the air-$CsPbBr_3$ boundary during its irradiation with a Gaussian-shaped laser pulse. f) Representative central cross-sectional AFM profile of a concave-shaped microcrater in $CsPbBr_3$ superimposed with geometric parabolic fit.

radial frequency of incident light. For $F \approx F_{th}$, such estimation gives comparable values of plasma density for both materials, N_{eh}(Si) = 1×10^{21}cm^{-3} and N_{eh}($CsPbBr_3$) = 0.6×10^{21}cm^{-3}. Remarkably, two-photon absorption in silicon with its coefficient (=2 cm per GW[42]) is almost negligible. At such high densities, the dominating recombination process is the Auger relaxation, because the electron-phonon relaxation in $CsPbBr_3$ is already saturated at 10^{19} cm^{-3}.[43] For electron-electron-hole Auger recombination, described by characteristic time τ_{AR}=(C×N$_{eh}^2$)$^{-1}$, we estimated τ_{AR}(Si) = 3.5 ps (at the Auger coefficient C = 2.8×10^{-31} cm^{6}s^{-1}[44]) and τ_{AR}($CsPbBr_3$) = 100 fs (at C = 5.3×10^{-28} cm^{6}s^{-1}[45]). When compared with that of Si, hot dense electron-hole plasma induced in the perovskite material can recombine three orders of magnitude faster, thus resulting in a much stronger localization within the region where carriers exchange energy with ions. Thermal capacity of Si (700 J kg^{-1}K^{-1}[46]) is higher that of $CsPbBr_3$ (280 J kg^{-1}K^{-1}[30]), which means that the perovskite requires less absorbed energy to be heated equally to Si. Finally, $CsPbBr_3$ possesses a much lower thermal conductivity (κ = 0.4 W m^{-1} K^{-1}[4]) than that of Si (κ = 130 W m^{-1} K^{-1}[46]), which leads to stronger heat localization in the perovskite after its lattice sub-system heated by carriers. As a result, because of its ultrafast electron-hole recombination rate and extremely low thermal conductivity, $CsPbBr_3$ exhibits an almost negligible heat penetration depth L_T. Fast thermalization and negligible heat spreading allow fs-laser pulses to locally remove the material from its exposed areas. Noteworthy, the sublimation temperature of $CsPbBr_3$ is ≈690 K (twice lower compared with that of Si), permitting to directly evaporate this material. Within such an ablation regime, generation of surface debris and nanoparticles

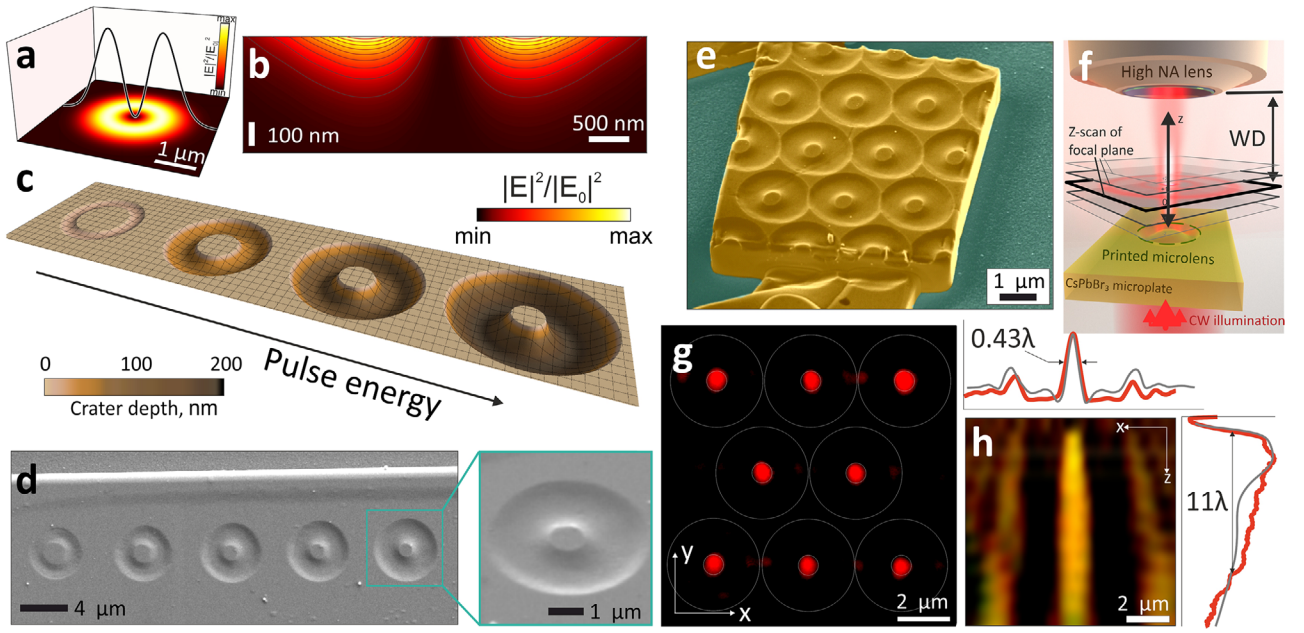

Figure 2. Laser printing of $CsPbBr_3$ micro-optical elements. a) Lateral intensity profile of a donut-shaped CVB. b) Normalized squared electric-field amplitude calculated near the air-$CsPbBr_3$ boundary during its irradiation with a CVB. c) Geometry of an ablated donut-shaped crater modeled for elevated laser fluence *F*. d) Top-view SEM images of donut-shaped microcraters produced at increased laser fluence *F*. Inset shows a side-view SEM image of a single microcrater. e) False-color SEM image of $CsPbBr_3$ microcrystals patterned with donut-shaped microcraters (truncated microaxicons) arranged into hexagonal lattice at a pitch size of 4 μm. f) Setup for optical characterization of the truncated microaxicons. g) Corresponding focal plate intensity distribution generated by a microaxicon array at 632 nm pump from bottom side. h) Measured axial intensity distribution in the single focal spot produced by a truncated perovskite microaxicon. Top and side insets provide measured (red) and calculated (gray) focal depth and focal-plane FWHM width of the Bessel-like beam generated by the axicon.

is substantially suppressed, which results in clean and precise patterning (see Figure 1d).

Taking into account the above mentioned features of laser-induced thermalization of $CsPbBr_3$, results of its surface ablation can be roughly predicted by calculating the squared electromagnetic field amplitude in the material $|E(r,z)|^2=|E(r)e^{-z\alpha}|^2$ that exceeds the threshold value $|E_{th}|^2$ required for ablation. In this case, the surface profile of microcrater is defined by the following equation:

$$z(r) = \frac{1}{2\alpha} ln\left(\frac{|E_{th}|^2}{|E(r)|^2}\right) \tag{1}$$

For a Gaussian-shaped laser beam with $E(r) = E_0 e^{-\left(\frac{r}{r_0}\right)^2}$, the laser-imprinted surface profile will follow the parabolic geometry defined by:

$$z(r) = \frac{1}{2\alpha} ln\frac{|E_{th}|^2}{|E_0|^2} + \frac{1}{\alpha}\left(\frac{r}{r_0}\right)^2 \tag{2}$$

This deduction is generally consistent with the results of finite-difference time domain (FDTD) calculations of the $|E(r,z)|^2$, as well as those of atomic-force microscopy (AFM), both confirming the parabolic-shaped profile of microcraters (Figure 1e,f).

Interestingly, similar full-wave electromagnetic simulations can also be applied to predict the result of the $CsPbBr_3$ ablation with more complicated laser beam profiles. Without loss of generality, we further considered another practically relevant case, that is, the perovskite exposure to a focused azimuthally polarized cylindrical vector beam (CVB) having a characteristic donut-shaped lateral intensity profile described in polar coordinates (ρ, φ) as follows (see **Figure 2**a and Supporting Information):

$$|E(\rho,\varphi)|^2 = k^2 f^2 \left| \int_0^{\beta} R(\theta) \begin{pmatrix} -iJ_1(k\rho\sin\theta)\sin\phi \\ iJ_1(k\rho\sin\theta)\cos\phi \\ 0 \end{pmatrix} \sqrt{\cos\theta}\,\sin\theta\, d\theta \right|^2 \tag{3}$$

where (θ, ϕ) are the spherical angular coordinates of the focusing system's output pupil, β is the maximum value of the azimuthal angle related to the system's numerical aperture NA = $n\sin\beta$ for a medium with the refraction index *n*, $R(\theta)$ is a complex amplitude function of the incident laser beam, $k = 2\pi/\lambda$ is the wavenumber, λ is the wavelength, f is the focal length of the focusing system, and $J_1(x)$ is the first-order Bessel function of the first kind.

In this case, laser ablation is expected to leave a similar donut-shaped crater on the $CsPbBr_3$ surface. For a fixed size of CVB, FDTD calculations allowed us to trace the evolution of surface profile at elevated applied laser fluence *F* as illustrated in Figure 2b,c. Remarkably, the calculated surface morphology almost perfectly fits that of the microcraters produced via single-pulse laser ablation of $CsPbBr_3$ with CVBs (Figure 2d). As seen in Figure 2b, by tuning the applied laser fluence *F*, one can

adjust the geometrical shape of the produced central protrusion. Similar to ablation with Gaussian-shaped laser pulses, the donut-shaped surface morphology imprinted with CVBs is perfectly reproducible from pulse to pulse, which permits to cover the entire microcrystal with a hexagonal array of microcraters (Figure 2e). Such surface features fabricated via a single-step procedure can act as an array of truncated microaxicons. The latter microaxicons were demonstrated to generate diffraction-limited Bessel-like beams upon being excited from the opposite side (see Figure 2f) as the $CsPbBr_3$ monocrystals used are completely transparent in the wavelength range ≥550 nm (see Supporting Information). By systematically testing focusing performance of such micro-optical elements, we found the spot size around 0.43 ± 0.03 μm (≈ 0.68λ at $\lambda = 632$ nm; full-width half-maximum value) generated at the focal distance of around ≈ 1 μm above the microcrystal surface (see Figure 2g,h). The axial intensity profile reconstructed from a series of snapshots along the optical axis indicates the formation of Bessel-like beam with a depth of focus (DoF) around 11λ. Focusing characteristics of the produced truncated microaxicons were also assessed using FDTD calculations which indicated good agreement with experimentally measured values (gray curves, Figure 2h). The resultant maximum numerical aperture of the microaxicon was found to be around NA = 0.8. Note that use of more complex CVBs can give an additional degree of freedom to design appropriate surface profiles of processed perovskite microcrystal and thus expand its applicability range. An interested reader is referred to Supporting Information where we made corresponding calculations of microlenses that can be imprinted by several types of high-order CVBs as well as assessed focusing performance of such micro-optical elements.

Note that the Abbe criterion defines the lateral size of focal spot as $\approx\lambda/2n_m$NA (where n_m is the refractive index of the medium focusing the laser radiation). In this case, when a laser pulse hits $CsPbBr_3$ microcrystal, the $n_m = 1$ owing to the corresponding boundary conditions at the flat interface. However, non-flat specially designed surface morphology is expected to couple laser radiation into the material and focus it therein. In this case, the minimal laser spot size will be improved by a factor that is equal to the refractive index of $CsPbBr_3$, $n_{CsPbBr3}$ (see **Figure 3**a–c). According to previous studies,[12] $n_{CsPbBr3}$=2.35 for the used microcrystals, which ensures 100-nm sized features that can be potentially produced in our material.

To prove the applicability of this concept, we first imprinted high-quality 2D gratings with a characteristic pitch size of 400 nm on the surface of $CsPbBr_3$ microcrystals (inset of Figure 3a). Fabrication was performed with a 0.4-μm width 15-μm long flat-top stripe-shaped laser beam generated using a projection lithography approach (see details in ref. [37]). Note that such precise laser processing regime can be applied to fabricate high-quality $CsPbBr_3$ surface gratings with a pitch size down to 250 nm and smooth morphology verified by AFM measurements (see Supporting Information).

Next, the surface grating was irradiated by a second linearly polarized laser pulse as illustrated in Figure 3b. FDTD calculations predict that depending on the orientation of the second-pulse polarization vector with respect to the trench orientation, the incident field couples the $CsPbBr_3$ grating in a very different way. In particular, for a TE-polarized beam (polarization vector is oriented along the imprinted trenches), each surface elevation acts as a microlens focusing incident radiation within an extremely confined spot just beneath the $CsPbBr_3$ surface (Figure 3c, top). Such a tight focusing is expected to increase the penetration depth of the laser into the perovskite material (in comparison with a flat perovskite surface; see Supporting Information). In a sharp contrast, similar exposure of the grating to a TM-polarized radiation is expected to deepen the imprinted trenches according to the FDTD calculations (Figure 3c, bottom).

Figure 3d demonstrates a $CsPbBr_3$ surface grating partially irradiated with a large (15×15 μm^2 in size) TE-polarized flat-top beam at F≈$1.1F_{th}$. As one can see, such irradiation left 75-nm wide nanoslits whose position coincides with the surface elevation of the initial grating, as was predicted by FDTD simulations. Next, we irradiated a similar 2D surface grating with a TE-polarized stripe-shaped beam (similar to those used to imprint the grating). The stripe orientation was set to be perpendicular with respect to the imprinted trenches, as illustrated in Figure 3e,f. Single-pulse (F ≈ $1.1F_{th}$) irradiation of the grating with such a beam was found to create linear arrays of elongated (100 × 200 nm^2) nano-pitches. By translating this beam with a fixed period of 400 nm, one can produce high-quality rectangular array of such nano-pitches. It should be noted that such processing with TM-polarized stripe-shaped beam only permits to imprint surface gratings oriented perpendicularly with respect to the initial trenches (Figure 3e). 3D morphology of the surface gratings imprinted with TE- and TM-polarized stripe-shaped beam is characterized by AFM scans shown in the Supporting Information. Figure 3g shows how the morphology of $CsPbBr_3$ surface evolves upon increasing the fluence of the second-pass TE-polarized laser beam from $1.05F_{th}$ to $1.2F_{th}$. Importantly, the appearance of nanoholes in between rectangular nano-pitches was also predicted by FDTD calculations that indicated formation of low-intense maxima of electromagnetic field imprinted at elevated fluence (Figure 3c). These results clearly illustrate how laser processing parameters govern the subwavelength $CsPbBr_3$ surface ablation whose behavior can be accurately predicted using direct FDTD calculations without involvement of complex and resource-consuming multiphysics calculations. Moreover, by gradually rotating the polarization orientation of laser pulses with respect to the imprinted trenches, one can precisely control ablation behavior at the nanoscale (see Supporting Information).

Figure 3h shows reference SEM and PL images (recorded at pump wavelength of 532 nm) of an isolated $CsPbBr_3$ microcrystal locally patterned with rectangular arrays of nano-pitches and demonstrating stronger PL yield (with respect to the pristine surface areas). This PL enhancement can be attributed to better coupling (out-coupling) of the pump (PL) radiation, as well as to the near-field localization of the incident radiation by nanoscale surface features. More importantly, this result shows that laser patterning did not deteriorate the PL properties of the processed $CsPbBr_3$ material. This opens pathways for facile noninvasive printing of surface morphologies that improve functionalities of perovskite microcrystals.[37] As an additional demonstration of this opportunity, we showed that by producing concave microcraters on the surface of $CsPbBr_3$ material, its lasing threshold can be substantially reduced owing to improved focusing of pump radiation inside the material (see Supporting Information). Moreover, direct laser pattering can be readily applied to imprint functional morphology not only on the surface of

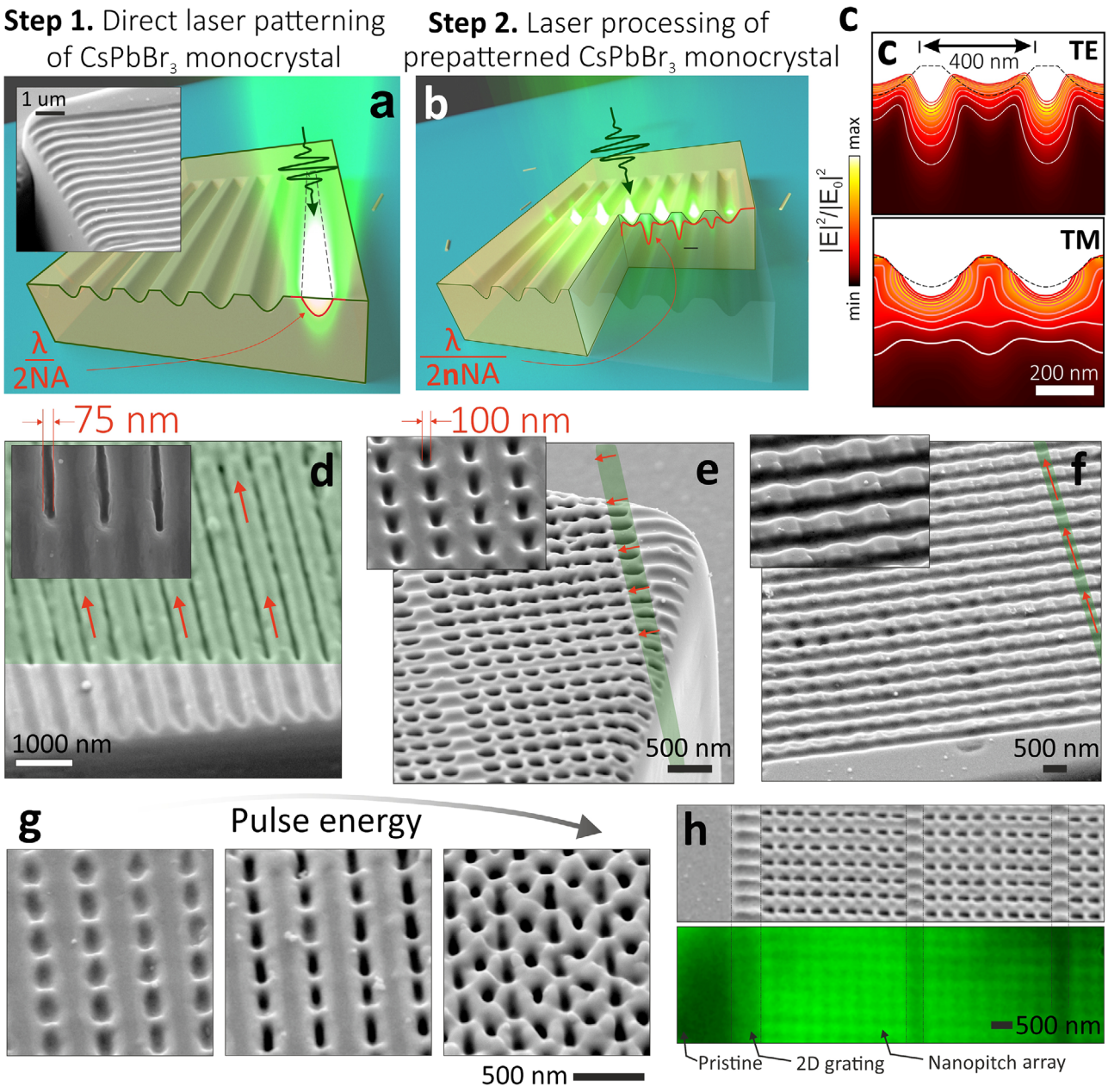

Figure 3. Two-step subwavelength laser processing of $CsPbBr_3$ micro-crystals. a,b) Schematic illustration of a two-step laser processing approach permitting to achieve better localization of laser radiation inside $CsPbBr_3$ microcrystal. Each pillar of the surface grating imprinted via direct laser ablation with a stripe-shaped beam enables better focusing and deeper penetration of subsequent laser pulses into processed $CsPbBr_3$. Inset in panel (a) demonstrates a side-view SEM image of $CsPbBr_3$ surface grating printed with stripe-shaped laser beam at a pitch of 400 nm. c) Squared electric-field amplitude $|E(r, z)|^2$ calculated near the $CsPbBr_3$ surface grating upon its irradiation by TE- and TM-polarized plane wave at 532 nm from the top. d) Side-view SEM image of a similar surface grating irradiated by a subsequent large flat-top laser beam. Inset presents an SEM image of produced nanoslits with a width of 75 nm. e,f) Side-view SEM images of similar surface gratings further processed with a stripe-shaped laser beam oriented perpendicularly with respect to the lines of the initial surface grating. The strip-shape beam has the lineal polarization perpendicular (TM; e) or along (TE; f) the initial surface grating orientation as schematically illustrated in both panels. Inset in panel (f) indicates formation of high-quality array of deep subwavelength pitches. g) Series of side-view SEM images showing evolution of the $CsPbBr_3$ surface morphology with elevated pulse energy during the second pass. The two-step fabrication with beam arrangement illustrated in panel (f) was used to produce these surface patterns. h) Reference SEM and PL images of isolated $CsPbBr_3$ microcrystal locally patterned with rectangular nanohole arrays.

laterally wide microplates but also atop more complicated chemically synthesized perovskite nanostructures—nanowires with a typically sub-micron width/height.[47] Such nanowires represent promising platform for realization of perovskite nanolasers,[48] while gentle post-modification of the surface morphology of as-synthesized nanostructures would open up pathways for improvement of their functional characteristics (lasing threshold, directivity, etc.). To highlight such remarkable modality of direct laser pattering we demonstrate fabrication of high-quality surface nanograting with a pitch size of 250 nm atop the isolated 45-μm long $CsPbBr_3$ nanowire (see Supporting Information). Our numerical simulations in Supporting Information confirm the improvement of coupling efficiency in such nanostructured waveguides, which makes them also prospective for integrated photonics and polaritonics.

3. Conclusion

In this work, we took advantage of the extremely low thermal conductivity of single-crystal $CsPbBr_3$ perovskite and its ultrafast thermalization rate (predominately dictated by Auger recombination of its photoexcited carriers) to realize precise and clean direct fs-laser processing of its surface. In particular, we create ultra-smooth micro-optic elements (as parabolic microlenses and truncated microaxicons) as well as more complex 2D and 3D morphologies (predicted by full-wave electromagnetic calculations) directly imprinted with deep subwavelength (down to $\lambda/7$) resolution on the surface of chemically synthesized $CsPbBr_3$ microplates. We believe that the developed approach can compete or even replace various standard multistage lithographic approaches applied for halide perovskites[18,49–51] to develop advanced micro-optoelectronic devices.[52–55]

Supporting Information

Supporting Information is available from the Wiley Online Library or from the author.

Acknowledgements

This work was supported by Russian Science Foundation (Grant No. 19-19-00177) regarding laser processing and characterization. A.Y.Z. and S.V.M. express their gratitude to the Ministry of Science and Higher Education of the Russian Federation (Grant Nos. MK-4200.2021.1.2. and 14.Y26.31.0010 for the samples synthesis).

Conflict of Interest

The authors declare no conflict of interest.

Data Availability Statement

Research data are not shared.

Keywords

ablation, femtosecond lasers, halide perovskites, luminescence, nanophotonics

Received: February 18, 2021
Revised: April 19, 2021
Published online: June 17, 2021

[1] https://www.nrel.gov/pv/cell-efficiency.html.
[2] M. Lu, Y. Zhang, S. Wang, J. Guo, W. W. Yu, A. L. Rogach, *Adv. Funct. Mater.* **2019**, 1902008.
[3] X. Yang, J. Wu, T. Liu, R. Zhu, *Small Methods* **2018**, *2*, 1800110.
[4] S. Makarov, A. Furasova, E. Tiguntseva, A. Hemmetter, A. Berestennikov, A. Pushkarev, A. Zakhidov, Y. Kivshar, *Adv. Opt. Mater.* **2019**, *7*, 1800784.
[5] A. S. Berestennikov, P. M. Voroshilov, S. V. Makarov, Y. S. Kivshar, *Appl. Phys. Rev.* **2019**, *6*, 031307.
[6] Y. Li, X. Zhang, H. Huang, S. V. Kershaw, A. L. Rogach, *Mater. Today* **2020**, *32*, 204.
[7] Y. Fu, H. Zhu, J. Chen, M. P. Hautzinger, X.-Y. Zhu, S. Jin, *Nat. Rev. Mater.* **2019**, *4*, 169.
[8] B. Gholipour, G. Adamo, D. Cortecchia, H. N. Krishnamoorthy, M. Birowosuto, N. I. Zheludev, C. Soci, *Adv. Mater.* **2017**, *29*, 1604268.
[9] S. V. Makarov, M. I. Petrov, U. Zywietz, V. Milichko, D. Zuev, N. Lopanitsyna, A. Kuksin, I. Mukhin, G. Zograf, E. Ubyivovk, D. A. Smirnova, S. Starikov, B. N. Chichkov, Y. S. Kivshar, *Nano Lett.* **2017**, *17*, 3047.
[10] Y. Cao, N. Wang, H. Tian, J. Guo, Y. Wei, H. Chen, Y. Miao, W. Zou, K. Pan, Y. He, H. Cao, Y. Ke, M. Xu, Y. Wang, M. Yang, K. Du, Z. Fu, D. Kong, D. Dai, Y. Jin, G. Li, H. Li, Q. Peng, J. Wang, W. Huang, *Nature* **2018**, *562*, 249.
[11] E. Tiguntseva, G. P. Zograf, F. E. Komissarenko, D. A. Zuev, A. A. Zakhidov, S. V. Makarov, Y. S. Kivshar, *Nano Lett.* **2018**, *18*, 1185.
[12] E. Y. Tiguntseva, D. G. Baranov, A. P. Pushkarev, B. Munkhbat, F. Komissarenko, M. Franckevicius, A. A. Zakhidov, T. Shegai, Y. S. Kivshar, S. V. Makarov, *Nano Lett.* **2018**, *18*, 5522.
[13] Y. Gao, C. Huang, C. Hao, S. Sun, L. Zhang, C. Zhang, Z. Duan, K. Wang, Z. Jin, N. Zhang, A. V. Kildishev, C.-W. Qiu, Q. Song, S. Xiao, *ACS Nano* **2018**, *12*, 8847.
[14] E. Tiguntseva, Z. Sadrieva, B. Stroganov, Y. V. Kapitonov, F. Komissarenko, R. Haroldson, B. Balachandran, W. Hu, Q. Gu, A. Zakhidov, A. Bogdanov, S. V. Makarov, *Appl. Surf. Sci.* **2019**, *473*, 419.
[15] C. Zhang, S. Xiao, Y. Wang, Y. Gao, Y. Fan, C. Huang, N. Zhang, W. Yang, Q. Song, *Laser Photonics Rev.* **2019**, 1900079.
[16] A. Berestennikov, Y. Li, I. Iorsh, A. Zakhidov, A. Rogach, S. Makarov, *Nanoscale* **2019**, *11*, 6747.
[17] Y. Fan, Y. Wang, N. Zhang, W. Sun, Y. Gao, C.-W. Qiu, Q. Song, S. Xiao, *Nat. Commun.* **2019**, *10*, 2085.
[18] K. Wang, G. Xing, Q. Song, S. Xiao, *Adv. Mater.* **2020**, 2000306.
[19] G. E. Eperon, D. Bryant, J. Troughton, S. D. Stranks, M. B. Johnston, T. Watson, D. A. Worsley, H. J. Snaith, *J. Phys. Chem. Lett.* **2014**, *6*, 129.
[20] W. Zhang, M. Anaya, G. Lozano, M. E. Calvo, M. B. Johnston, H. Míguez, H. J. Snaith, *Nano Lett.* **2015**, *15*, 1698.
[21] K. Deng, L. Li, *Small Methods* **2019**, 1900150.
[22] Q. Zhang, M. M. Tavakoli, L. Gu, D. Zhang, L. Tang, Y. Gao, J. Guo, Y. Lin, S.-F. Leung, S. Poddar, *Nat. Commun.* **2019**, *10*, 727.
[23] S. Chen, K. Roh, J. Lee, W. K. Chong, Y. Lu, N. Mathews, T. C. Sum, A. Nurmikko, *ACS Nano* **2016**, *10*, 3959.
[24] A. Y. Vorobyev, C. Guo, *Laser Photonics Rev.* **2013**, *7*, 385.
[25] C. Kerse, H. Kalaycıoğlu, P. Elahi, B. Çetin, D. K. Kesim, Ö. Akçaalan, S. Yavaş, M. D. Aşık, B. Öktem, H. Hoogland, *Nature* **2016**, *537*, 84.
[26] O. Tokel, A. Turnalı, G. Makey, P. Elahi, T. Çolakoğlu, E. Ergeçen, Ö. Yavuz, R. Hübner, M. Z. Borra, I. Pavlov, A. Bek, R. Turan, D. K. Kesim, S. Tozburun, S. Ilday, F. Ö. Ilday, *Nat. Photonics* **2017**, *11*, 639.

[27] M. Malinauskas, A. Žukauskas, S. Hasegawa, Y. Hayasaki, V. Mizeikis, R. Buividas, S. Juodkazis, *Light: Sci. Appl.* **2016**, *5*, e16133.
[28] A. Sergeev, D. Pavlov, A. Kuchmizhak, M. Lapine, W. Yiu, Y. Dong, N. Ke, S. Juodkazis, N. Zhao, S. Kershaw, A. L. Rogach, *Light: Sci. Appl.* **2020**, *9*, 1.
[29] D. Bäuerle, *Laser Processing and Chemistry*, Springer Science & Business Media, Berlin, Heidelberg**2013**.
[30] T. Haeger, R. Heiderhoff, T. Riedl, *J. Mater. Chem. C* **2020**, *8*, 14289.
[31] G. Mincuzzi, A. L. Palma, A. Di Carlo, T. M. Brown, *ChemElectroChem* **2016**, *3*, 9.
[32] L. Bayer, M. Ehrhardt, P. Lorenz, S. Pisoni, S. Buecheler, A. N. Tiwari, K. Zimmer, *Appl. Surf. Sci.* **2017**, *416*, 112.
[33] L. Bayer, X. Ye, P. Lorenz, K. Zimmer, *Appl. Phys. A* **2017**, *123*, 619.
[34] C. Zhou, G. Cao, Z. Gan, Q. Ou, W. Chen, Q. Bao, B. Jia, X. Wen, *ACS Appl. Mater. Interfaces* **2019**, *11*, 26017.
[35] A. Zhizhchenko, S. Syubaev, A. Berestennikov, A. V. Yulin, A. Porfirev, A. Pushkarev, I. Shishkin, K. Golokhvast, A. A. Bogdanov, A. A. Zakhidov, Y. kivshar, S. Makarov, *ACS Nano* **2019**, *13*, 4140.
[36] I. Shishkin, A. Polushkin, E. Tiguntseva, A. Murzin, B. Stroganov, Y. Kapitonov, S. A. Kulinich, A. Kuchmizhak, S. Makarov, *Appl. Phys. Express* **2019**, *12*, 122001.
[37] A. Y. Zhizhchenko, P. Tonkaev, D. Gets, A. Larin, D. Zuev, S. Starikov, E. V. Pustovalov, A. M. Zakharenko, S. A. Kulinich, S. Juodkazis, A. A. Kuchmizhak, S. V. Makarov, *Small* **2020**, *16*, 2000410.
[38] Z. Wang, T. Yang, Y. Zhang, Q. Ou, H. Lin, Q. Zhang, H. Chen, H. Y. Hoh, B. Jia, Q. Bao, *Adv. Mater.* **2020**, 2001388.
[39] J. Bonse, S. Baudach, J. Krüger, W. Kautek, M. Lenzner, *Appl. Phys. A* **2002**, *74*, 19.
[40] N. A. Smirnov, S. I. Kudryashov, P. A. Danilov, A. A. Rudenko, A. A. Ionin, A. A. Nastulyavichus, *JETP Letters* **2018**, *108*, 368.
[41] D. E. Aspnes, A. Studna, *Phys. Rev. B* **1983**, *27*, 985.
[42] D. Reitze, T. Zhang, W. M. Wood, M. C. Downer, *JOSA B* **1990**, *7*, 84.
[43] T. R. Hopper, A. Jeong, A. Gorodetsky, F. Krieg, M. I. Bodnarchuk, X. Huang, R. Lovrincic, M. V. Kovalenko, A. A. Bakulin, *Phys. Chem. Chem. Phys.* **2020**.
[44] A. Richter, S. W. Glunz, F. Werner, J. Schmidt, A. Cuevas, *Phys. Rev. B* **2012**, *86*, 165202.
[45] N. Droseros, G. Longo, J. C. Brauer, M. Sessolo, H. J. Bolink, N. Banerji, *ACS Energy Lett.* **2018**, *3*, 1458.
[46] R. Hull, *Properties of Crystalline Silicon*, vol. 20, IET, Stevenage, UK**1999**.
[47] A. P. Pushkarev, V. I. Korolev, D. I. Markina, F. E. Komissarenko, A. Naujokaitis, A. Drabavicius, V. Pakstas, M. Franckevicius, S. A. Khubezhov, D. A. Sannikov, *ACS Appl. Mater. Interfaces* **2018**, *11*, 1040.
[48] H. Zhu, Y. Fu, F. Meng, X. Wu, Z. Gong, Q. Ding, M. V. Gustafsson, M. T. Trinh, S. Jin, X. Zhu, *Nat. Mater.* **2015**, *14*, 636.
[49] J. Harwell, J. Burch, A. Fikouras, M. C. Gather, A. Di Falco, I. D. Samuel, *ACS Nano* **2019**, *13*, 3823.
[50] C. Zou, C. Chang, D. Sun, K. F. Böhringer, L. Y. Lin, *Nano Lett.* **2020**, *20*, 3710.
[51] D. Xing, C.-C. Lin, Y.-L. Ho, A. S. A. Kamal, I.-T. Wang, C.-C. Chen, C.-Y. Wen, C.-W. Chen, J.-J. Delaunay, *Adv. Funct. Mater.* **2021**, *31*, 1 2006283.
[52] N. Zhang, W. Sun, S. P. Rodrigues, K. Wang, Z. Gu, S. Wang, W. Cai, S. Xiao, Q. Song, *Adv. Mater.* **2017**, *29*, 1606205.
[53] P. Cegielski, A. L. Giesecke, S. Neutzner, C. Porschatis, M. Gandini, D. Schall, C. Perini, J. Bolten, S. Suckow, S. Kataria, B. Chmielak, T. Wahlbrink, A. Petrozza, M. Lemme, *Nano Lett.* **2018**, *18*, 6915.
[54] P. Trofimov, A. P. Pushkarev, I. S. Sinev, V. V. Fedorov, S. Bruyere, A. Bolshakov, I. S. Mukhin, S. V. Makarov, *ACS Nano* **2020**, *14*, 8126.
[55] H. Gu, S.-C. Chen, Q. Zheng, *Adv. Opt. Mater.* **2021**, *9*, 2001637.